Original Article

Preliminary study of cine-MRI compression in MR-guided radiotherapy

Jiawen Shang[#], Peng Huang[#], Ke Zhang[#], Zhihui Hu, Hui Yan

Department of Radiation Oncology, National Cancer Center/National Clinical Research Center for Cancer/Cancer Hospital, Chinese Academy of Medical Sciences and Peking Union Medical College, Beijing, China

Contributions: (I) Conception and design: J Shang, P Huang, K Zhang; (II) Administrative support: H Yan; (III) Provision of study materials or patients: P Huang, K Zhang; (IV) Collection and assembly of data: P Huang; (V) Data analysis and interpretation: J Shang; (VI) Manuscript writing: All authors; (VII) Final approval of manuscript: All authors.

[#]These authors contributed equally to this work and should be considered as co-first authors.

Correspondence to: Hui Yan, PhD. Department of Radiation Oncology, National Cancer Center/National Clinical Research Center for Cancer/Cancer Hospital, Chinese Academy of Medical Sciences and Peking Union Medical College, Beijing 100021, China. Email: hui.yan@cicams.ac.cn.

Background: Cine-magnetic resonance imaging (MRI) is currently used in real-time tumor tracking during magnetic resonance (MR)-guided radiotherapy. As a type of MRI specified for motion tracking, a few minutes' acquisition results in thousands of 2-dimensional (2D) images. For MR-guided radiotherapy consisting of multiple treatment fractions, the large number of cine-MRI images would be disproportionate to the tight clinical data storage available. To alleviate this issue, the feasibility of compression of cine-MRI via video encoders was investigated in this study.

Methods: The cine-MRI images were first sorted into 3 sequences according to their plane orientations. Then, each sequence was reordered according to their acquisition times [time-based (TB)] or content similarities [similarity-based (SB)]. As a result, 3 sequences were obtained for 3 plan orientations. Next, the obtained sequences were processed by a video encoder and the corresponding 3 video files were achieved. We employed 3 popular video encoders: Motion JPEG (M-JPEG), Advanced Video Coding (AVC), and High Efficiency Video Coding (HEVC). The performances of the sequence reordering methods and video encoders were evaluated based on a total of 150 image sets.

Results: The mean correlation quantities for SB sequences were higher than those for TB sequences by 3% (sagittal), 2% (coronal), and 1% (transverse), respectively. The average compression ratio (CR) yielded by the SB sequences was higher than that achieved by the TB sequences. Comparing with M-JPEG, the CRs obtained by AVC and HEVC were increased by 58% and 62% (sagittal), 16% and 23% (coronal), and 48% and 56% (transverse), respectively. Among the 3 video encoders, the highest CRs and restoration accuracy were achieved by HEVC.

Conclusions: HEVC with inter-frame coding is more effective in reducing the redundant information in consecutive images. It is feasible to implement the video encoder for high-performance cine-MRI compression.

Keywords: Cine-magnetic resonance imaging (cine-MRI); magnetic resonance-guided radiotherapy (MR-guided radiotherapy); data storage; compression; video encoder

Submitted May 17, 2023. Accepted for publication Aug 30, 2023. Published online Sep 18, 2023.
doi: 10.21037/qims-23-690
View this article at: https://dx.doi.org/10.21037/qims-23-690

Introduction

Magnetic resonance imaging (MRI) is a non-invasive imaging technology used for disease detection, diagnosis, and treatment monitoring. It is based on a sophisticated principle of excitation and detection of the change in the direction of the rotational axis of proton magnetic moment found in the water that makes up living tissues (1,2). MRI offers excellent soft tissue contrast for the precise identification of target volume and immediate detection of inter- and intra-fractional changes of the tumor and adjacent organs at risk. Differing from computed tomography (CT) and integrated cone-beam CT (CBCT) and megavoltage fan-beam CT (MV FBCT), the ionizing radiation of X-ray is not used in MRI (3,4). Recently a new radiotherapy machine, Unity (Elekta Solutions AB, Stockholm, Sweden), that combines MRI with linear accelerators, has become clinically available (5,6). It is composed of a 1.5T MRI scanner and a ring-based gantry containing a 7 MV linear accelerator, which enables online magnetic resonance (MR)-guided radiotherapy (7,8).

The new MR-Linac systems (Elekta) not only offer superior anatomical 3-dimensional (3D) imaging to detect inter-fractional changes, but also provide real-time information by continuous 2-dimensional (2D) cine-MRI, allowing for constant monitoring of tumor volume and nearby critical structures during the entire treatment session (9). For tumor tracking, a key frame of the cine-MRI is selected and registered to the volumetric image via deformable image registration. All subsequent cine-MRI images are registered to this key frame, which enables tracking of the target structure delineated in the volumetric image (10). Also, a 3D motion model could be established via deformation of the existing 3D/4-dimensional (4D) CT/MRI with the real-time cine-MRI (11,12). High-frequency cine-MRI could improve the target dose delivery and organ-at-risk (OAR) dose sparing. However, this means that a huge number of images will be generated in a short period of time (13). Cine-MRI acquired in a frequency of 5 Hz will result in 300 images per minute. These images are stored in a local computer and deleted after a few months in order to free more disk space for clinical applications. Although these data are not as critical as those of computed tomography (CT) and MRI, they contain important information of real-time changes of patient anatomical structures and should be handled properly for potential clinical and research uses.

Compression algorithms can significantly reduce the size yet preserve the original contents of the image. There are 2 types of compression algorithms: lossless and lossy (14). A lossless compression algorithm is reversible, which means that the original image information is preserved after image restoration. Lossless encoders include Huffman coding and Context-based Adaptive Binary Arithmetic Coding (CABAC) (15). A lossy compression algorithm is irreversible, meaning that the original image information is partially restored after decompression. A lossy encoder aims to retain as much of the original information as possible in order to compress the image (16).

Differing from image compression, video compression packs a series of images into a single file. Video compression can be categorized into intra- and inter-frame coding algorithms. An intra-frame coding algorithm processes each frame independently and handles redundancy of information inside a frame, such as the Motion JPEG (M-JPEG) algorithm (17). The inter-frame encoding algorithm takes into account redundant information among consecutive frames (18). Among the inter-frame coding algorithms, Advanced Video Coding (AVC) and High Efficiency Video Coding (HEVC) are the most popular standards. HEVC is the successor of AVC and provides an even higher compression rate while retaining the high video quality (19).

Different to 3D CT/MRI images, the cine-MRI consists of a series of 2D images acquired at a fixed plane. High-frequency MRI gives both the temporal resolution necessary for fully tracking respiratory motion and superior single-modality soft-tissue contrast required for imaging tumors in real-time (11). The most promising application of 2D cine-MRI is real-time tumor tracking using 2D-to-2D or 2D-to-3D template matching algorithms (20,21). It offers advantages in higher imaging frequency and soft tissue contrast over radiographic imaging. So far, it is an on-board imaging tool in addition to the 3D MRI in MR-guided radiotherapy and could improve the target dose delivery and OAR dose sparing by tracking internal markers directly.

Our attempts to apply conventional video encoders for CT, 4DCT, and CBCT were reported in our previous studies (22-24). Unlike these 3D images, cine-MRI is based on different image generation principles and consists of a series of images acquired at the fixed 2D plane. Therefore, the more effective reordering methods and video encoders should be applied and investigated. This manuscript is arranged as follows. In the methods section, the data acquisition of cine-MRI in MR-guided radiotherapy is first introduced. Then, the clustering algorithm for sequence reordering is explained. Next, the workflow of cine-MRI

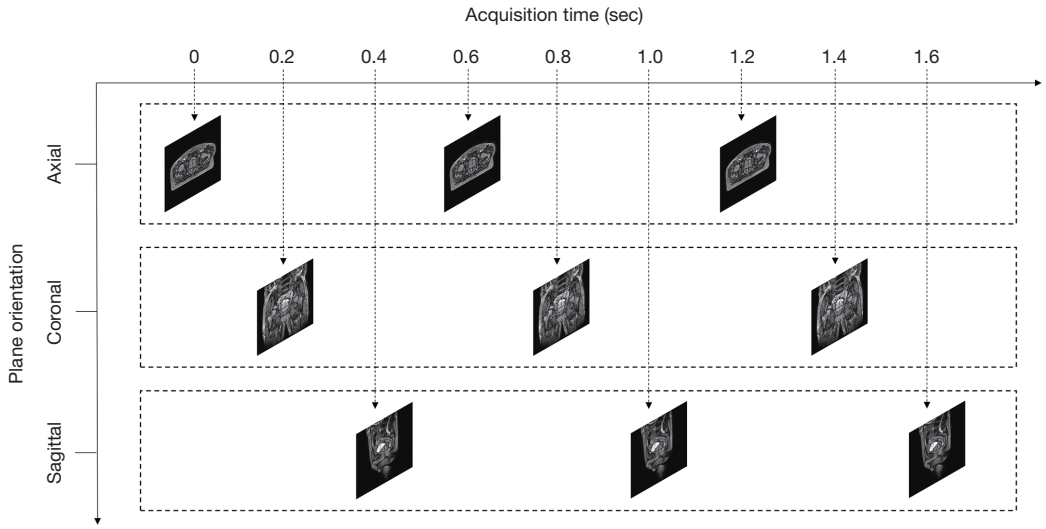

Figure 1 Illustrations of cine-MRI data acquisition process. MRI, magnetic resonance imaging.

compression and 3 video encoders are described. In the results section, the performance of sequence reordering methods and video encoders are analyzed and evaluated quantitatively.

Methods

Data acquisition

The datasets in this study were collected on a Unity system which was installed in our institute in 2018 (25). The pulse sequence used for cine-MRI in the clinical mode is a gradient echo pulse sequence, balanced turbo field echo (BTFE), with a balanced gradient waveform after an initial preparation pulse for contrast enhancement, yielding a T2/T1-weighted contrast (26). Right before the start of treatment, a preview cine-MRI scan is acquired for automated selection of a tracking key frame based on deformable image registration of a certain number of preview frames to the corresponding slice of the volumetric scan. During treatment, the live cine-MRI frames are in turn registered to the key frame, and the target is deformed based on the obtained deformation vector field (DVF). If in any frame the target is outside the specified margin, the beam will be turned off (27).

As shown in *Figure 1*, 1 cine-MRI sequence consists of a series of 2D planar images in 3 orthogonal views. These images were usually saved in raw data format in a folder. The plane orientation and acquisition time of cine-MRI images can be extracted from file headers and used for image reordering. In practice, these images are first classified into 3 groups according to their plane orientations, and then all images in each group are connected to form a sequence according to their acquisition times. As a result, 3 sequences corresponding to transverse, sagittal, and coronal planes are obtained as the image sequences inside the dot box as shown in *Figure 1*. These sequences are called time-based (TB) sequences in the following.

As cine-MRI images are highly correlated in space and time, it could be utilized to improve the inter-frame similarity of a sequence and ultimately cause a higher compression ratio (CR) of video encoder. Especially for the inter-frame coding algorithms, the higher correlation between consecutive frames in a sequence could result in a higher CR. Accordingly, it would be beneficial to reorder a sequence with lower inter-frame similarity to a new sequence with higher inter-frame similarity for better compression performance of video encoders. This study was conducted in accordance with the Declaration of Helsinki (as revised in 2013) and was approved by the institutional Ethics Committee of the Cancer Hospital, Chinese Academy of Medical Sciences, and Peking Union Medical College. The requirement for informed consent was waived in this retrospective study.

Reordering sequence

In this study, a sequence reordering algorithm based on

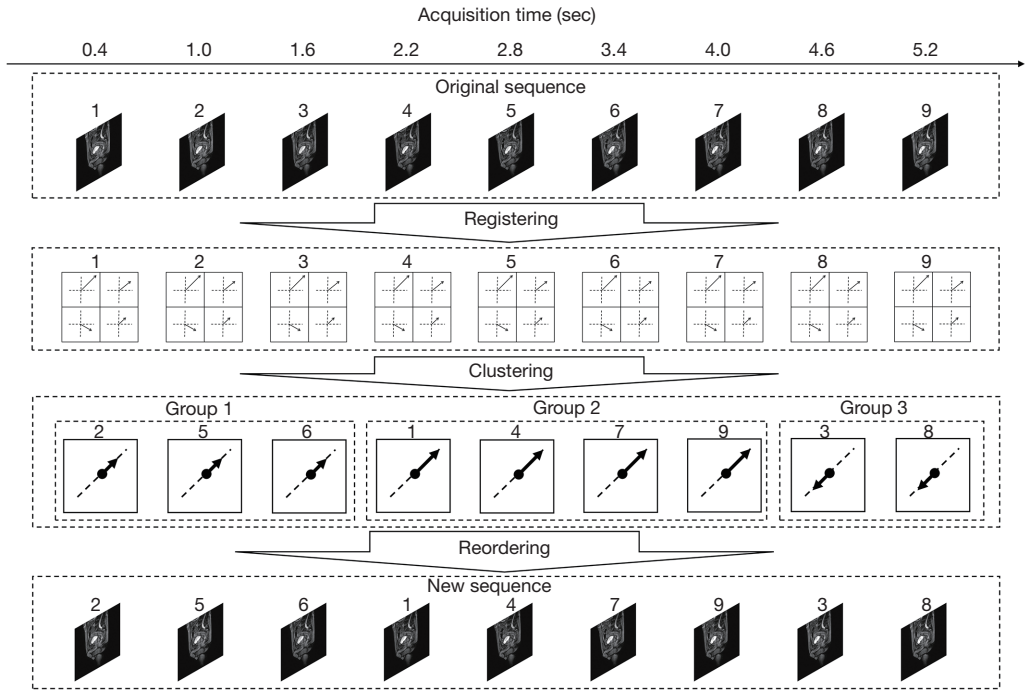

Figure 2 Illustrations of the similarity-based sequence reordering algorithm.

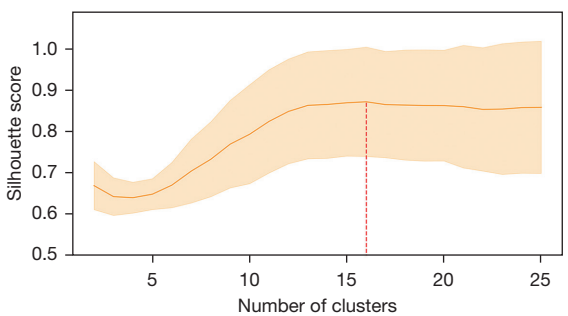

Figure 3 The curves of SIL with respect to the different number of clusters. The middle curve is the mean values of SIL, and the upper and lower curves are the standard deviation of SIL. The best cluster number [16] is indicated by the vertical dot line. SIL, Silhouette score.

respiratory movement was developed, and its workflow is shown in *Figure 2*. At first, the reference image is generated based on the mean image of a sequence and divided into 4×4 blocks. Then, the correlation quantities between the blocks at the same location in the reference and input images are calculated based on the grid partitioning algorithm as described in Appendix 1. These correlation quantities render the feature vector to represent the relative target motion of the input image as the step "registering" shown in *Figure 2*. Next, these feature vectors are processed by K-mean clustering algorithm to group them into different clusters as the step "clustering" shown in *Figure 2*. Silhouette score (SIL) is used to decide the number of clusters and the best number is 16. As shown in *Figure 3*, this number provides the best tradeoff with the higher mean and lower standard deviation of SIL.

The image in each group is assigned a tuple, including the unique group ID and the original image ID. Then, all images in a group are connected based on their original image IDs and all groups are connected based on their group IDs in ascending order as the step "reordering" shown in *Figure 2*. The new ID of an image in the sequence is also recorded in the tuple and used for data restoration. The new sequence is formed based on the similarities among images and called similarity-based (SB) sequence in the following.

Video encoders

The workflow of image compression from images to video files is shown in *Figure 4A*. Cine-MRI images are first classified into 3 groups based on their plane orientations.

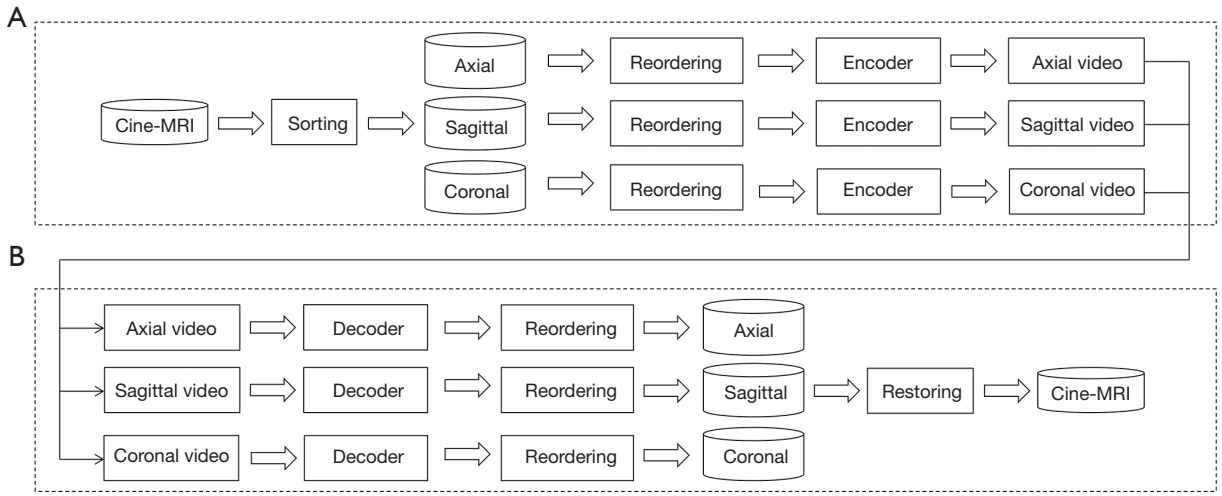

Figure 4 The workflow of image compression and decompression of cine-MRI. (A) Image compression. (B) Image decompression. MRI, magnetic resonance imaging.

Then, they are reordered to 3 sequences and processed by a video encoder. Finally, 3 video files are generated corresponding to transverse, sagittal, and coronal planes, respectively. The workflow of image decompression from video files to images is shown in *Figure 4B* and is the reverse process of compression. The 3 video files are first decoded to 3 image sequences corresponding to transverse, sagittal, and coronal planes. Then, the images within each sequence are restored to their original orders. Finally, these images are moved to a destination folder according to their original image IDs.

In this study, we tested 3 video encoders (M-JPEG, AVC, and HEVC). M-JPEG is a video compression format in which each video frame of a digital video sequence is compressed separately as a JPEG image (15-17). M-JPEG is an intra-frame compression scheme. Due to the lack of inter-frame prediction, its CR is relatively lower compared with modern inter-frame video formats such as MPEG-1, MPEG-2, and MPEG-4. AVC is based upon the MPEG-4 technology and the golden standard in video compression so far. AVC also called H.264 or MPEG-4 Part 10. HEVC is the latest international standard for video compression and the successor of AVC. HEVC is also called H.265. Distinct from AVC that sets all blocks in the same size, HEVC uses the customized size for all blocks. As a result, HEVC provides substantially improved video quality at the same bit rate over AVC (19,22-24).

Experiments

The 3 video encoders were tested on 2 types of sequences resulted by TB and SB algorithms as described above. A personal computer equipped with Intel i5 CPU 2.6 GHz and 8 GB RAM was used for these tests. The routines for data processing are developed with Python programming language (https://www.python.org/) and an open-source audio and a video converter tool, ffmpeg (https://ffmpeg.org/), was used as API for video compression. The default configuration is selected for M-JPEG to allow video data to be compressed as much as possible. The constant rate factor (CRF), the quality control setting for the encoders, is set to 25 for AVC and HEVC. Lower CRF would result in better quality at the expense of higher file sizes. The default values of CRFG for AVC and HEVC are 23 and 28, respectively.

CR is defined as the ratio between the sizes of image sequence and the resulting video file. The inter-frame difference (IF-DIFF) is used to quantify the mean pixel differences for all pairs of neighboring images in a sequence (20).

$$IF-DIFF=\frac{1}{L-1}\sum_{k=1}^{L-1}\left(\frac{\sum_{i=1}^{M}\sum_{j=1}^{N}\left|I_{ij}^{k}-I_{ij}^{k+1}\right|}{M\times N}\right) \quad [1]$$

Where M and N are the height and width of image, L is the number of images in a sequence, and I_{ij}^{k} is the pixel (i,j) in image k. The inter-frame correlation (IF-CORR) is used to quantify the mean correlation coefficient for all pairs of

Table 1 Performance comparison of the three video encoders on time-based sequences

Encoders	Views	CR	MSE	PSNR	VQM
M-JPEG	Sagittal	34.96±3.41	4.60E–05±4.39E–06	43.00±1.46	1.68E–2±3.97E–3
	Coronal	30.03±1.70	5.67E–05±3.92E–06	47.11±1.75	3.04E–2±6.27E–3
	Transverse	48.65±3.54	3.11E–05±3.54E–06	43.21±2.60	3.08E–2±1.07E–2
AVC	Sagittal	54.86±6.26	3.96E–05±4.01E–06	47.78±1.77	1.52E–2±3.62E–3
	Coronal	35.43±2.36	4.67E–05±3.66E–06	44.07±1.57	2.61E–2±5.61E–3
	Transverse	71.07±5.17	2.67E–05±3.45E–06	44.70±2.20	2.43E–2±7.10E–3
HEVC	Sagittal	55.81±6.58	3.10E–05±3.61E–06	48.86±1.75	1.29E–2±3.00E–3
	Coronal	37.86±2.91	3.93E–05±2.90E–06	44.72±1.53	2.37E–2±5.10E–3
	Transverse	75.46±6.58	1.93E–05±1.92E–06	45.62±2.52	2.16E–2±7.36E–3

Data are presented as mean ± standard deviation. CR, compression ratio; MSE, mean square error; PSNR, peak signal-to-noise ratio; VQM, video quality matrix; M-JPEG, Motion JPEG; AVC, Advanced Video Coding; HEVC, High Efficiency Video Coding.

neighboring images in a sequence (20).

$$IF-CORR=\frac{1}{L-1}\sum_{k=1}^{L-1}\left(\frac{\sum_{i=1}^{M}\sum_{j=1}^{N}\left(I_{ij}^{k}-\overline{I^{k}}\right)\left(I_{ij}^{k+1}-\overline{I^{k+1}}\right)}{\sqrt{\sum_{i=1}^{M}\sum_{j=1}^{N}\left(I_{ij}^{k}-\overline{I^{k}}\right)^{2}}\sqrt{\sum_{i=1}^{M}\sum_{j=1}^{N}\left(I_{ij}^{k+1}-\overline{I^{k+1}}\right)^{2}}}\right) \quad [2]$$

$\overline{I^{k}}$ and $\overline{I^{k+1}}$ are the mean values of images I^{k} and I^{k+1}. The correlation coefficient between I^{k} and I^{k+1} is defined by the equation inside the bracket.

The quantities, mean square error (MSE), peak signal-to-noise ratio (PSNR), and video quality matrix (VQM) are used to evaluate the restoration accuracy of image decompression. The MSE quantify the difference between the original and restored images after image restoration (26).

$$MSE=\frac{1}{L}\sum_{i=1}^{L}\left(\frac{\sum_{i=1}^{M}\sum_{j=1}^{N}\left(\overline{I_{ij}^{k,de}}-\overline{I_{ij}^{k}}\right)^{2}}{M\times N}\right) \quad [3]$$

$\overline{I_{ij}^{k}}$ is the normalized image and $\overline{I_{ij}^{k,de}}$ is the normalized image after decompression. PSNR is the ratio between the maximum power of a signal and the power of corrupting noise which is defined as below (26).

$$PSNR=10\cdot\log_{10}\left(\frac{MAX^{2}}{MSE}\right)[dB] \quad [4]$$

MAX is 216-1 which is the maximum value for a 16-bit image and its typical values are between 60 and 80 dB for a 16-bit image. VQM is the metric to quantify human perceived video quality defined as below (26).

$$VQM=\frac{1}{1+e^{\alpha(PSNR-b)}} \quad [5]$$

Where a=0.15 and b=19.7818 are determined experimentally.

Results

Performance of video encoders

The performances of the 3 video encoders on TB sequences are compared in *Table 1*. On average, the CR of AVC and HEVC was higher than that of M-JPEG. Among the 3 video encoders, HEVC had the highest CRs for both reordering methods. The CRs of 3 types of sequences were different and the transverse sequences had the highest CRs. Compared with M-JPEG, CRs obtained by AVC were increased by 58% (sagittal), 16% (coronal), and 48% (transverse), whereas CRs obtained by HEVC were increased by 62% (sagittal), 23% (coronal), and 56% (transverse). The improvement of CR by HEVC was more than that of AVC.

The restoration accuracy of 3 video encoders is shown in *Table 1*. The restoration accuracy of M-JPEG was inferior to those of AVC and HEVC. Among the 3 video encoders, HEVC had the best restoration accuracy. The restoration accuracies were different between the 3 anatomical planes and the transverse plane has the least MSEs. Compared with MSEs yielded by M-JPEG, those yielded by AVC were decreased by 14% (sagittal), 18% (coronal), and 14% (transverse), whereas those yielded by HEVC were decreased by 33% (sagittal), 31% (coronal), and 38% (transverse). The improvement of restoration accuracy by HEVC is more than that of AVC.

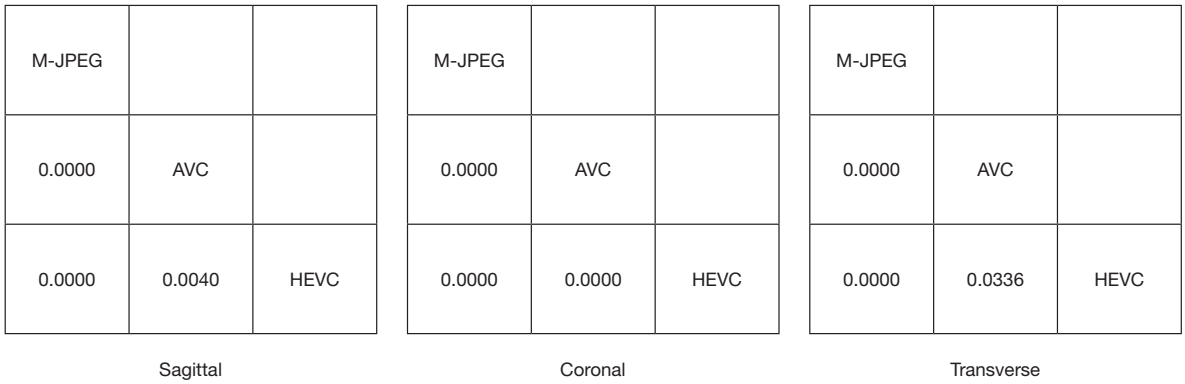

Figure 5 The corrected P values for multiple comparisons in evaluating the compression performance of M-JPEG, AVC, and HEVC on time-based sequences. M-JPEG, Motion JPEG; AVC, Advanced Video Coding; HEVC, High Efficiency Video Coding.

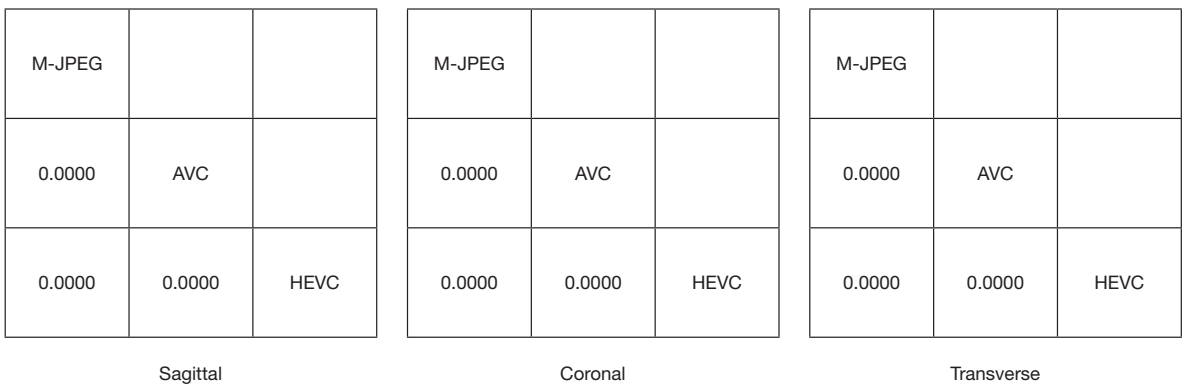

Figure 6 The corrected P values for multiple comparisons in evaluating the restoration accuracy of M-JPEG, AVC, and HEVC on time-based sequences. M-JPEG, Motion JPEG; AVC, Advanced Video Coding; HEVC, High Efficiency Video Coding.

The corrected P values for CR difference among the 3 video encoders based on 150 TB sequences are shown in *Figure 5*. A P value <0.05 was considered statistically significant. The improvements of CRs by AVC and HEVC were statistically significant compared to those of M-JPEG. The increase of CR by HEVC was statistically significant compared to that of AVC. HEVC had the highest CR among 3 video encoders. The corrected P values for MSE different among the video encoders based on 150 TB sequences are shown in *Figure 6*. The decreases of MSEs by AVC and HEVC were statistically significant compared to that of M-JPEG. The decreases of MSEs by HEVC were statistically significant compared to that of AVC. HEVC had the lowest MSE among the 3 video encoders.

Effect of reordering methods

The similarity metrics (IF-DIFF and IF-CORR) were calculated over 3 types of sequences in 2 ordering methods. The mean values of IF-DIFF for TB sequences were 117.26±14.43 (sagittal), 195.87±25.09 (coronal), and 158.26±31.31 (transverse), whereas the mean values of IF-DIFF for SB sequences were 92.80±6.69 (sagittal), 191.17±20.46 (coronal), and 156.21±28.35 (transverse). The mean values of IF-CORR for TB sequences were 0.93±0.01 (sagittal), 0.85±0.02 (coronal), and 0.90±0.03 (transverse), whereas the mean values of IF-CORR for SB sequences were 0.96±0.01 (sagittal), 0.87±0.03 (coronal), and 0.91±0.03 (transverse). In general, the mean values of IF-DIFF on all 3 types of sequences were 157.13±40.45 and 146.72±45.61 with TB and SB ordering methods, respectively. The mean values of IF-CORR on all 3 types of sequences were 0.89±0.04 and 0.91±0.04 with TB and SB ordering methods, respectively. Thus, the values of these similarity metrics for SB sequences were higher than those for the TB sequences.

The performances of the 3 video encoders on SB

Table 2 Performance comparison of the three video encoders on similarity-based sequences

Encoders	Views	CR	MSE	PSNR	VQM
M-JPEG	Sagittal	34.96±3.41	4.60E−05±4.39E−06	43.00±1.46	1.68E−2±3.97E−3
	Coronal	30.03±1.70	5.67E−05±3.92E−06	47.11±1.75	3.04E−2±6.27E−3
	Transverse	48.65±3.54	3.11E−05±3.54E−06	43.21±2.60	3.08E−2±1.07E−2
AVC	Sagittal	55.93±5.66	3.84E−05±3.93E−06	47.92±1.74	1.49E−2±3.51E−3
	Coronal	35.88±2.40	4.68E−05±3.65E−06	44.07±1.57	2.61E−2±5.64E−3
	Transverse	72.83±5.79	2.69E−05±3.25E−06	44.66±2.24	2.45E−2±7.34E−3
HEVC	Sagittal	58.06±6.19	3.02E−05±3.44E−06	48.97±1.68	1.27E−2±2.87E−3
	Coronal	38.33±2.94	3.88E−05±3.09E−06	44.71±1.46	2.37E−2±4.88E−3
	Transverse	75.73±7.38	1.91E−05±2.14E−06	45.70±2.46	2.13E−2±7.05E−3

Data are presented as mean ± standard deviation. CR, compression ratio; MSE, mean square error; PSNR, peak signal-to-noise ratio; VQM, video quality matrix; M-JPEG, Motion JPEG; AVC, Advanced Video Coding; HEVC, High Efficiency Video Coding.

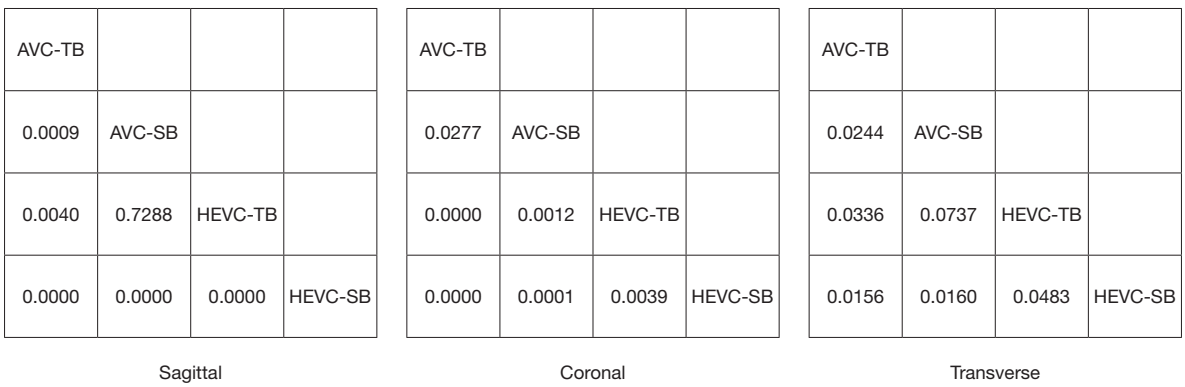

Figure 7 The corrected P values for multiple comparison in evaluating compression performance of AVC and HEVC with respect to time-based and similarity-based sequence reordering methods. AVC, Advanced Video Coding; TB, time-based; SB, similarity-based; HEVC, High Efficiency Video Coding.

sequences are compared in *Table 2*. Note that the result of M-JPEG is the same at those of *Table 1*. This is because the intra-frame coding algorithm processes each image independently regardless of the ordering methods of images. In general, the CR of AVC and HEVC on SB sequences was higher than those of them on TB sequences. As shown in *Table 2*, the restoration accuracy of AVC and HEVC on SB sequences is similar to those on TB sequences.

The corrected P values for CRs of AVC and HEVC with 2 reordering methods on 150 sequences are shown in *Figure* 7. A P value <0.05 was considered statistically significant. The improvement of CRs achieved by SB sequences was statistically significant compared to those achieved by TB sequences. The CRs by HEVC were consistently higher than those by AVC for both sequence reordering methods. The corrected P-values for MSE of AVC and HEVC with respect to 2 sequence reordering methods based on 150 sequences are shown in *Figure 8*. The decreases of MSEs yielded by SB sequences were statistically significant compared to those yielded by TB sequences. The MSEs achieved by HEVC were consistently less than those obtained by AVC.

Discussion

It was found that the CR of video encoders with the inter-frame coding algorithm was consistently higher than the video encoder with an intra-frame coding algorithm.

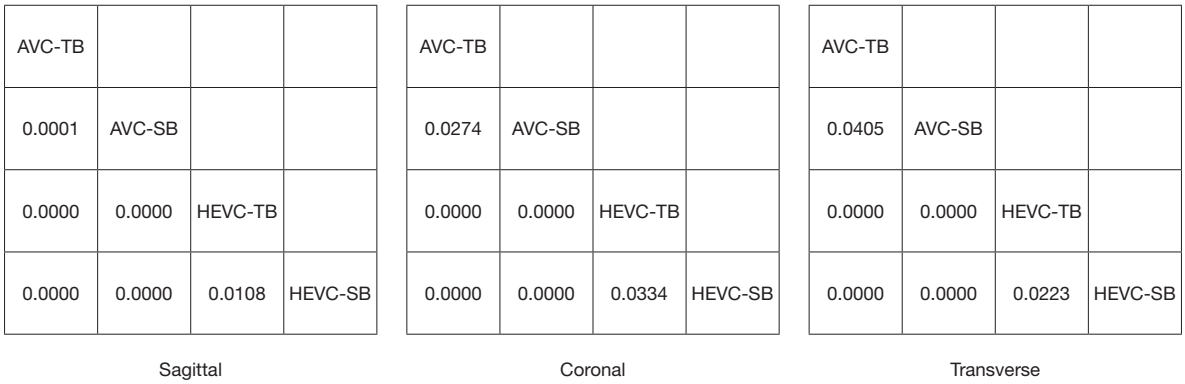

Figure 8 The corrected P values for multiple comparison in evaluating restoration accuracy of AVC and HEVC with respect to time-based and similarity-based sequence reordering methods. AVC, Advanced Video Coding; TB, time-based; SB, similarity-based; HEVC, High Efficiency Video Coding.

This indicates that the redundancy among frames can be effectively reduced by the prediction mechanism employed in inter-frame coding algorithms (22-24). For medical images such as CT and MRI, this continuity is a natural property that exists in spatial space. Therefore, it is favorable to use video encoders with an inter-frame coding algorithm for medical image compression.

The advanced video encoders could provide an even higher CR. In this study, the CRs of AVC were 41.3% and 43.7% higher than those of M-JPEG based on TB and SB sequences, respectively. HEVC demonstrated even higher CRs than those of M-JPEG by 43.5% and 51.2% based on TB and SB sequences, respectively. The CRs of HEVC were also 4.8% and 5.1% higher than those of AVC based on TB and SB sequences, respectively. Compared to our previous results (18-20), the CRs achieved by AVC for cine-MRI were relatively low. The reason for this may be that more bony structures and less noise are usually presented in 4DCT and CBCT, whereas a large quantity of noise, contrast difference, and deformation of soft tissues usually appear in cine-MRI. The poor IF-CORR between slices could have resulted from these factors (15).

The clustering algorithm was introduced in sequence reordering of this study to improve the inter-frame similarity of the sequences for video encoding. The similarity metrics were evaluated and compared for both TB and SB methods. In general, the SB reordering method showed better performance than the TB reordering method. This indicates that improving similarity between 2 adjacent slices in a sequence could be beneficial for higher CR. However, as the motion region is smaller relative to the whole image in this study, the improvement of inter-frame similarity of a sequence is small.

As the amplitudes and directions of organ motion in 3 cardinal planes are different, the inter-frame similarities of their sequences and the subsequent CRs of their videos are varied. Among them, the average CR of transverse sequences is the highest, and the average CRs of the sagittal and coronal sequences are the second and third, respectively. This indicates that the motion amplitude of organ is the least in transverse plane followed by the sagittal plane. The proposed clustering algorithm can capture the organ motion information in which the inter-frame coding algorithms can be utilized.

M-JPEG with intra-frame encoder took the least time in terms of the processing time. This is because the intra-fame coding algorithm does not deal with the correlation computation and motion prediction between frames. Meanwhile, more time is spent on block searching, motion vector prediction, data interpolation, in the video encoders with inter-frame coding algorithm. It should be noted that the time spent on compression could increase significantly with the advanced video encoder. For example, the time spent by AVC was 1.18 times that spent by M-JPEG, whereas the time spent by HEVC was 4.05 times that spent by M-JPEG. As a consequence, the additional processing time will result in higher CRs and restoration accuracy.

The effect of decompression loss on the clinical use of cine-MRI could be minor as the main clinical application of cine-MRI is for real-time tumor/target tracking and it is less frequently used for treatment planning purposes (20,21). For retrospective reviewing purposes, it could be used to

build a 3D motion model via deformable transformation of 4DCT or 3DCT (11,12). Similar to 2D KV/MV images or 3D CBCT which are routinely used in tumor localization and position verification during radiotherapy treatment, the image quality requirement for cine-MRI is not higher than those of 3D CT/MRI which are acquired for diagnosis, surgical simulation, and treatment planning purposes. In our previous study (24), the influence of decompression loss on target localization accuracy was evaluated based on decompressed images and the results showed that its impact was hardly discernible. The effect of decompression loss on the clinical applications of cine-MRI should be investigated in the same way as our previous studies. Considering that substantial effort is required for the multiple image registration tasks (2D-to-2D and 2D-to-3D) to be evaluated in 3 cardinal views for a patient, this work will be continued in our future study.

Conclusions

The inter-frame coding algorithm provides an efficient way to store cine-MRI for MRI-guided radiotherapy. The storage space can be significantly reduced while the major content of the image can be effectively conserved. For cine-MRI, the SB sequence reordering method provides a better way for further improving current compression performance. Among the 3 video encoders, HEVC provided the best performance with the highest CR and restoration accuracy, making it a better choice for clinical on-board image data storage.

Acknowledgments

Funding: This work was partially supported by the National Natural Science Foundation of China (No. 11975312) and Beijing Municipal Natural Science Foundation (No. 7202170).

Footnote

Conflicts of Interest: All authors have completed the ICMJE uniform disclosure form (available at https://qims.amegroups.com/article/view/10.21037/qims-23-690/coif). The authors have no conflicts of interest to declare.

Ethical Statement: The authors are accountable for all aspects of the work in ensuring that questions related to the accuracy or integrity of any part of the work are appropriately investigated and resolved. The study was conducted in accordance with the Declaration of Helsinki (as revised in 2013). The institutional Ethics Committee of the Cancer Hospital, Chinese Academy of Medical Sciences, and Peking Union Medical College approved this study. The requirement for informed consent was waived in this retrospective study.

References

1. Yousaf T, Dervenoulas G, Politis M. Advances in MRI Methodology. Int Rev Neurobiol 2018;141:31-76.
2. Pommier P, Gassa F, Lafay F, Claude L. Image guided radiotherapy with the Cone Beam CT kV (Elekta): experience of the Léon Bérard centre. Cancer Radiother 2009;13:384-90.
3. Bergom C, Prior P, Kainz K, Morrow NV, Ahunbay EE, Walker A, Allen Li X, White J. A phase I/II study piloting accelerated partial breast irradiation using CT-guided intensity modulated radiation therapy in the prone position. Radiother Oncol 2013;108:215-9.
4. Witt JS, Rosenberg SA, Bassetti MF. MRI-guided adaptive radiotherapy for liver tumours: visualising the future. Lancet Oncol 2020;21:e74-82.
5. Henke LE, Contreras JA, Green OL, Cai B, Kim H, Roach MC, Olsen JR, Fischer-Valuck B, Mullen DF, Kashani R, Thomas MA, Huang J, Zoberi I, Yang D, Rodriguez V, Bradley JD, Robinson CG, Parikh P, Mutic S, Michalski J. Magnetic Resonance Image-Guided Radiotherapy (MRIgRT): A 4.5-Year Clinical Experience. Clin Oncol (R Coll Radiol) 2018;30:720-7.
6. Fischer-Valuck BW, Henke L, Green O, Kashani R, Acharya S, Bradley JD, et al. Two-and-a-half-year clinical experience with the world's first magnetic resonance image guided radiation therapy system. Adv Radiat Oncol 2017;2:485-93.
7. Raaymakers BW, Jürgenliemk-Schulz IM, Bol GH, Glitzner M, Kotte ANTJ, van Asselen B, et al. First

patients treated with a 1.5 T MRI-Linac: clinical proof of concept of a high-precision, high-field MRI guided radiotherapy treatment. Phys Med Biol 2017;62:L41-50.
8. Raaymakers BW, Lagendijk JJ, Overweg J, Kok JG, Raaijmakers AJ, Kerkhof EM, van der Put RW, Meijsing I, Crijns SP, Benedosso F, van Vulpen M, de Graaff CH, Allen J, Brown KJ. Integrating a 1.5 T MRI scanner with a 6 MV accelerator: proof of concept. Phys Med Biol 2009;54:N229-37.
9. Green OL, Rankine LJ, Cai B, Curcuru A, Kashani R, Rodriguez V, Li HH, Parikh PJ, Robinson CG, Olsen JR, Mutic S, Goddu SM, Santanam L. First clinical implementation of real-time, real anatomy tracking and radiation beam control. Med Phys 2018. [Epub ahead of print]. doi: 10.1002/mp.13002.
10. Spindeldreier CK, Klüter S, Hoegen P, Buchele C, Rippke C, Tonndorf-Martini E, Debus J, Hörner-Rieber J. MR-guided radiotherapy of moving targets. Radiologe 2021;61:39-48.
11. Keiper TD, Tai A, Chen X, Paulson E, Lathuilière F, Bériault S, Hébert F, Cooper DT, Lachaine M, Li XA. Feasibility of real-time motion tracking using cine MRI during MR-guided radiation therapy for abdominal targets. Med Phys 2020;47:3554-66.
12. Dasnoy-Sumell D, Aspeel A, Souris K, Macq B. Locally tuned deformation fields combination for 2D cine-MRI-based driving of 3D motion models. Phys Med 2022;94:8-16.
13. Garau N, Via R, Meschini G, Lee D, Keall P, Riboldi M, Baroni G, Paganelli C. A ROI-based global motion model established on 4DCT and 2D cine-MRI data for MRI-guidance in radiation therapy. Phys Med Biol 2019;64:045002.
14. Brennecke R, Bürgel U, Rippin G, Post F, Rupprecht HJ, Meyer J. Comparison of image compression viability for lossy and lossless JPEG and Wavelet data reduction in coronary angiography. Int J Cardiovasc Imaging 2001;17:1-12.
15. Noreña T, Romero E. Medical image compression: a review. Biomedica 2013;33:137-51.
16. Selvathi D, Thayammal S. A Review on Transform Based Image Compression Techniques. International Journal of Engineering Research & Technology 2013;2.
17. 45 - JPEG and motion-JPEG (M-JPEG) compression. In: Poynton C, editor. Digital Video and HD. Second edition. Boston: Morgan Kaufmann; 2012:491-504.
18. Nosratinia A, Mohsenian N, Orchard MT, Liu B. Interframe coding of magnetic resonance images. IEEE Trans Med Imaging 1996;15:639-47.
19. Malhotra M, Singh AV, Matam R. Comparative Performance Issues with H.264 vs H.265. 2019 International Conference on Machine Learning, Big Data, Cloud and Parallel Computing (COMITCon), Faridabad, India; 2019:283-8.
20. Cerviño LI, Du J, Jiang SB. MRI-guided tumor tracking in lung cancer radiotherapy. Phys Med Biol 2011;56:3773-85.
21. Ozhasoglu C, Murphy MJ. Issues in respiratory motion compensation during external-beam radiotherapy. Int J Radiat Oncol Biol Phys 2002;52:1389-99.
22. Yan H, Li Y, Dai J. Four-Dimensional Cone-Beam Computed Tomography Image Compression Using Video Encoder for Radiotherapy. J Digit Imaging 2020;33:1292-300.
23. Yan H, Li Y, Dai J. Exploring correlation information for image compression of four-dimensional computed tomography. Quant Imaging Med Surg 2019;9:1270-7.
24. Yan H, Li Y, Dai J. Evaluation of video compression methods for cone-beam computerized tomography. J Appl Clin Med Phys 2019;20:114-21.
25. Zhang K, Tian Y, Li M, Men K, Dai J. Performance of a multileaf collimator system for a 1.5T MR-linac. Med Phys 2021;48:546-55.
26. Bieri O, Scheffler K. Fundamentals of balanced steady state free precession MRI. J Magn Reson Imaging 2013;38:2-11.
27. Xia WL, Liang B, Men K, Zhang K, Tian Y, Li MH, Lu NN, Li YX, Dai JR. Prediction of adaptive strategies based on deformation vector field features for MR-guided adaptive radiotherapy of prostate cancer. Med Phys 2023;50:3573-83.

Cite this article as: Shang J, Huang P, Zhang K, Hu Z, Yan H. Preliminary study of cine-MRI compression in MR-guided radiotherapy. Quant Imaging Med Surg 2023;13(12):8009-8019. doi: 10.21037/qims-23-690

Appendix 1 Supplementary methods

Grid partitioning algorithm

To analyze the correlation between regions on the images more precisely, a grid partitioning algorithm was employed in this study.

At first, the reference image is established based on the mean image $\overline{X}$ of all frames in a sequence. Then, a rectangular grid is used to divide reference image into multiple square blocks, called reference blocks, $T=\{T_{0,0},\cdots,T_{j,k},\cdots,T_{G,G}\},0\le j,k<G$ with the size $T_{j,k}\in R^{w\times h}$ as shown in Figure S1A. Similarly, each input frame X_i was divided into multiple square blocks, called frame blocks, $E^i=\{E^i_{0,0},\cdots,E^i_{j,k},\cdots,E^i_{G,G}\},0\le j,k<G$ with the size $E^i_{j,k}\in R^{W\times H},W>w,H>h$ as shown in Figure S1B. Compared to the size of the reference block, the size of the frame block is enlarged to account for more respiratory motion induced change of image content. In this study, the grid size G is 4.

As shown in Figure S1, the frame block $E^i_{m,n}$ in frame X_i corresponds to the reference block $T_{j,k}$ in reference image $\overline{X}$. The template matching algorithm traverses the reference block to calculate the relative offset $v^i_{j,k}$ between the reference block and the overlapping frame block. As a result, each frame X_i can obtain a matrix $v^i=\{v^i_{0,0},\cdots,v^i_{j,k},\cdots,v^i_{G,G}\}$ which represents the relative shifts of blocks of each frame to their counterparts of reference image. This matrix serves as a feature vector to represent the local respiratory motion of each frame and used by the subsequent clustering algorithm.

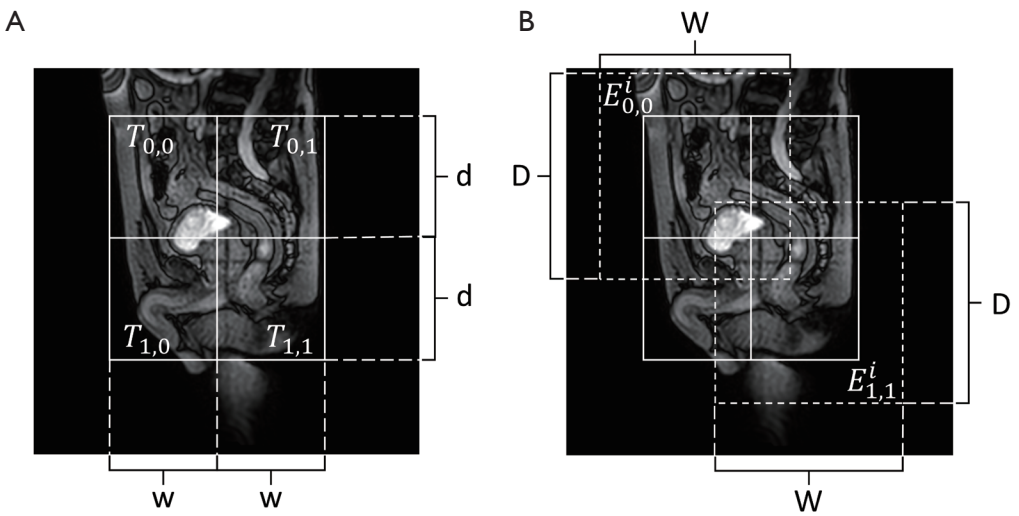

Figure S1 The illustration of square blocks in reference and frame images. (A) Reference blocks. (B) Frame blocks.

https://dx.doi.org/10.21037/qims-23-690